

Article

Detection of Forest Disturbances with Different Intensities Using Landsat Time Series Based on Adaptive Exponentially Weighted Moving Average Charts

Tingwei Zhang ¹, Ling Wu ^{1,*}, Xiangnan Liu ¹, Meiling Liu ¹, Chen Chen ², Baowen Yang ¹, Yuqi Xu ¹ and Suchang Zhang ¹

¹ The School of Information Engineering, China University of Geoscience, Beijing 100083, China; 2104210084@email.cugb.edu.cn (T.Z.); liuxn@cugb.edu.cn (X.L.); liuml@cugb.edu.cn (M.L.); yangbaowen163@163.com (B.Y.); xuyuqi2021@163.com (Y.X.); 2104200083@cugb.edu.cn (S.Z.)

² The Land Satellite Remote Sensing Application Center, MNR, Beijing 100048, China; chenchen_gis@hotmail.com

* Correspondence: wuling@cugb.edu.cn; Tel.: +86-138-1141-0374

Abstract: Forest disturbance detection is important for revealing ecological changes. Long-time series remote sensing analysis methods have emerged as the primary approach for detecting large-scale forest disturbances. Many of the existing change detection algorithms focus primarily on identifying high-intensity forest disturbances, such as harvesting and fires, with only a limited capacity to detect both high-intensity and low-intensity forest disturbances. This study proposes an online continuous change detection algorithm for the detection of multi-intensity forest disturbances such as forest harvest, fire, selective harvest, and insects. To initiate the proposed algorithm, the time series of the Normalized Difference Vegetation Index (NDVI) is fitted into a harmonic regression model, which is then followed by the computation of residuals. Next, the residual time series is entered into the adaptive exponentially weighted moving average (AEWMA) chart. This chart adaptively adjusts the smoothing coefficients to identify both high-intensity and low-intensity disturbances. When the chart value consistently deviates from the control limit, the forest pixel is classified as disturbed. With an overall spatial accuracy of 85.2%, including 86.1% producer's accuracy and 84% user's accuracy, along with a temporal accuracy of 96.7%, the algorithm enables precise and timely detection of forest disturbances with multiple intensities. This method provides a robust solution for detecting multi-intensity disturbances in forested regions.

Keywords: change detection; multi-intensity forest disturbances; landsat time-series; AEWMA chart



Citation: Zhang, T.; Wu, L.; Liu, X.; Liu, M.; Chen, C.; Yang, B.; Xu, Y.; Zhang, S. Detection of Forest Disturbances with Different Intensities Using Landsat Time Series Based on Adaptive Exponentially Weighted Moving Average Charts. *Forests* **2024**, *15*, 19. <https://doi.org/10.3390/f15010019>

Academic Editor: Giorgos Mallinis

Received: 20 November 2023

Revised: 13 December 2023

Accepted: 18 December 2023

Published: 20 December 2023



Copyright: © 2023 by the authors. Licensee MDPI, Basel, Switzerland. This article is an open access article distributed under the terms and conditions of the Creative Commons Attribution (CC BY) license (<https://creativecommons.org/licenses/by/4.0/>).

1. Introduction

Forests currently play a pivotal role in the global carbon cycle, biodiversity preservation, and environmental monitoring [1]. However, they are susceptible to disturbances resulting from climate change, human activities, and various other factors [2–5]. The disturbance of forests elucidates the process of forest evolution and the development of forest ecosystems, exerting a fundamental influence on the ecological environment [6–9]. The advancement of science and technology has enabled remote sensing to supplant manual investigations as the primary tool for Earth observation and the detection of large-scale terrestrial ecosystem changes, making it an effective method for quantitative analysis and the characterization of surface change processes [10]. Since the U.S. Geological Survey (USGS) made Landsat datasets accessible, these resources have found extensive use, particularly in large-scale change detection studies [11,12]. This access presents a valuable opportunity to gain a more comprehensive understanding of changes on Earth. Acquiring timely information on forest disturbances using remote sensing time series is pivotal for sustainable

forest management, carbon accounting, ecosystem management, and the exploration of ecological shifts and vegetation recovery [13].

Time series change detection methods can identify the characteristics, trends, and development patterns of changes in images. Most pixel-based remote sensing change detection methods are post-classification methods [14] and direct detection methods [15]. Post-classification comparison methods involve conducting a classification and subsequently comparing the results with those of a previous image to identify any changes that may have occurred. However, these methods are limited by the accuracy of the classification results. The direct detection method identifies pixel changes directly using specific indicators or thresholds, such as Landsat-based detection of trends in disturbance and recovery (LandTrendr) [16], Breaks for additive seasonality and trend (BFAST) [17], and the continuous change detection and classification algorithm (CCDC) [18]. The LandTrendr algorithm employs images captured during the same season to mitigate the influence of seasonal variations on change detection outcomes [16,19]. While LandTrendr excels at capturing long-term trends, it introduces discontinuities in the time series and may slightly delay the detection of sub-annual changes due to its use of annual images obtained only once per year. Therefore, several algorithms encompass fitting harmonic regression models to extract the residual time series and identify intra-annual alterations [17,18,20]. The BFAST [17,21] algorithm iteratively dissects the time series into seasonal, trend, and residual components, and it has been widely employed for high-intensity disturbances such as fire and harvest [22–25]. In addition, the Continuous Monitoring of Forest Disturbance Algorithm (CMFDA) [26] employs a harmonic regression model to mitigate phenological changes, enabling the detection of forest disturbances at high temporal frequencies by identifying pixels with three consecutive changes as disturbances. Building upon the CMFDA, the CCDC [18] Continuous Monitoring of Land Disturbance (COLD) algorithm [27] was subsequently developed. Both of them extend the capability for continuous detection of multiple land cover changes.

However, most of the aforementioned methods are tailored for the detection of high-intensity disturbances, and errors significantly escalate in the presence of multiple disturbance types with varying intensities [28]. For instance, while the COLD algorithm can detect disturbances with varying intensities, it still exhibits relatively high omission errors for low-intensity disturbances [27]. The effective detection of low-intensity disturbances is pivotal in identifying multi-intensity disturbances and has emerged as a prominent and well-acknowledged topic in recent years [29,30]. Zhao et al. [31] proposed an algorithm that detects not only high-intensity but also low-intensity disturbances, which are difficult to obtain by single-best-model algorithms. However, high-intensity disturbances will have lower accuracy as the data gets noisier. Brooks et al. [20,32] introduced a change detection algorithm that applies the exponentially weighted moving average (EWMA) chart to identify subtle disturbances in forest degradation and thinning. The EWMA Change Detection (EWMACD) is sensitive to low-intensity disturbances when the smoothing coefficient λ that determines the threshold for detecting changes is small. However, in cases of sudden and severe disturbances, a small λ may result in a delay effect in detecting high-intensity disturbances. It means a single EWMA chart with a fixed λ cannot well detect low- and high-intensity disturbances simultaneously. In summary, the current change detection algorithms for single-intensity (high- or low-intensity) forest disturbances cannot well detect multi-intensity forest disturbances. synchronously; however, the simultaneous occurrence of multi-intensity forest disturbances in the same area is common.

The aim of this study is to construct a change detection algorithm for detecting multiple intensities of forest disturbances. Capizzi and Masarotto introduced an adaptive EWMA (AEWMA) chart [33], which can adaptively adjust λ to enhance shift identification and improve robustness [34,35]. This study is to introduce an AEWMA change detection (AEWMACD) algorithm designed to facilitate the detection of multi-intensity forest disturbances. The detected disturbance agents in this article include both high-intensity disturbances (harvest and fire) and low-intensity disturbances (selective harvest and insects). Through

comparing it with the EWMACD algorithm, the ability of AEWMACD to detect various disturbance agents was evaluated, and the differences in detection accuracy among these agents were analyzed.

2. Study Area and Data

2.1. Study Area

This study area is situated in two representative counties, Jingzhou and Tongdao, in the southwestern part of Hunan Province, China, characterized by a significant forest cover (Figure 1). In 2021, the local statistical offices in these two counties reported forest cover percentages of 74.93% and 77.24%, respectively. This region's forest ecosystem is fragile and highly susceptible to disturbances, owing to its distinctive karst landscape, soil conditions, extreme climate, forest insects and diseases, human activities, and other contributing factors. The primary agents of forest disturbance targeted in this study encompass deforestation (such as harvest and selective harvest), insects, and fire, leading to different change magnitudes in the forest's spectral characteristics. Consequently, this study area offers an ideal setting for assessing the feasibility of detecting a wide range of disturbance agents within Landsat time series data using the proposed AEWMACD algorithm.

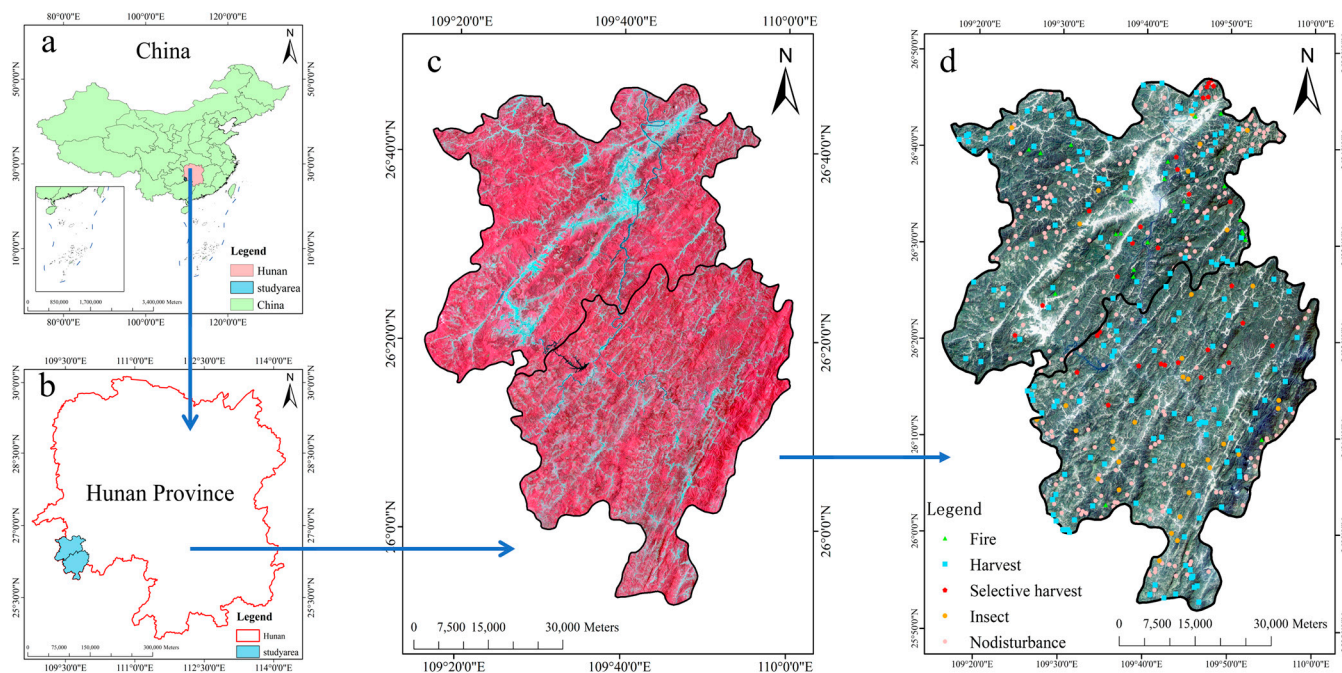


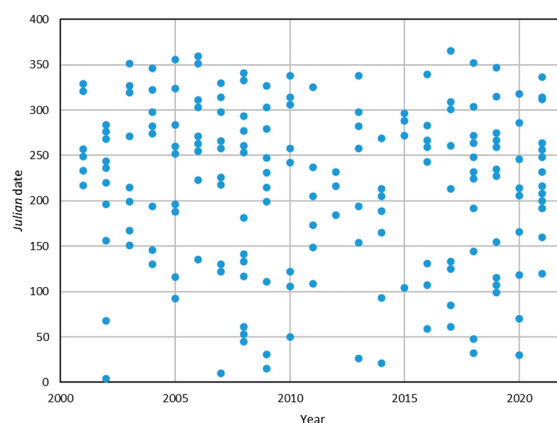
Figure 1. Geographic location and Landsat image of this study area: (a) general location within China, (b) within Hunan Province, (c) Landsat8 OLI false-color composite image (RGB = near-infrared, red, and green band), and (d) validation data selected in this area.

2.2. Data

The algorithm employed Landsat data, which offers a medium spatial resolution (30 m) and a long archival period spanning over 50 years [36]. Specifically, Landsat5 TM data, Landsat7 ETM+ data, and Landsat8 OLI data were utilized. Over the period from 2001 to 2021, a total of 177 surface reflectance (SR) products were procured from the USGS (Table 1), ensuring that the proportion of contaminated pixels remained below 60% (Figure 2). To mitigate the scan line corrector (SLC) malfunction experienced by Landsat7 since 2003, interpolation was conducted using the ENVI plugin. A forest benchmark mask was generated by employing a random forest classification algorithm, utilizing the Landsat image captured on 3 October 2002. The Normalized Difference Vegetation Index (NDVI) was computed and served as the input for the algorithm.

Table 1. Information on data and validation data.

Data Type	Acquisition Date (Sum)	Resolution	Sources
Landsat	5 (TM) 7 (ETM+) 8 (OLI)	30 m	USGS
MOD14A1 (Version 6.1)	14 September 2001–25 August 2011 (48)	1000 m	MODIS (USGS/GEE)
High-resolution data	5 August 2001–2 December 2021 (88) 13 July 2013–8 November 2021 (41) 18 February 2000 to Present 3 May 2003 to Present	-	Google Earth PRO Manual
Validation data	5 August 2001–2 December 2021	Vector	Interpretation; Statistical Data; News

**Figure 2.** Temporal distribution of available images with less than 60% of contaminated pixels between 2001 and 2021.

2.3. Validation Data

Due to the absence of other remote sensing images with both higher temporal and finer spatial resolution than Landsat images spanning from 2001 to 2021, the most reliable and optimal source for assessing the accuracy of forest disturbance detection based on Landsat time series is the Landsat images themselves [18,37]. To ensure the judicious selection of samples for this study, we employed a range of methodologies, including visual interpretation through Google Earth, consultation of statistical data and news sources, and the utilization of existing partial datasets such as the MODIS fire detection dataset (MOD14A1) (Table 1). Consequently, we meticulously curated a total of 500 reference samples from these images, evenly distributed between undisturbed forest areas and areas experiencing disturbances, with 250 samples in each category (Figure 1d).

In the process of validation data selection, the first step are spatial coordinate matching. Google Earth data, statistical data, and forest disturbance news all directly acquire the latitude and longitude of the disturbance point and then match them to the Landsat image. However, since the resolution of the MODIS fire dataset (MOD14A1) are lower than that of Landsat, the corresponding range on the Landsat image is found according to the latitude and longitude of MOD14A1, and then the fire pixel on Landsat is determined by manual interpretation. The second step is temporal matching. MODIS products, statistical data, and news all directly acquire the time information and then match the nearest Landsat image backward. However, due to the restricted temporal precision of available high-resolution images (usually spanning one or two years), manual interpretation are applied to Google Earth data. This process begins with an examination of the chosen disturbance pixels and their occurrence times on Google Earth data. Subsequently, a comparative analysis is conducted with the disturbance pixels in Landsat images taken before and after the disturbance time, facilitating the determination of disturbance timing on Landsat imagery. These disturbance samples are classified into four types, grouped into two primary categories: high-intensity (harvest and fire) and low-intensity (insect and selective harvest),

as depicted in Figure 3a. In the absence of disturbances, the time-series curve should demonstrate a cyclic pattern, as denoted by the dashed line in Figure 3b,c. However, when a disturbance occurs, the curve deviates from this regular pattern, as illustrated by the dotted lines in Figure 3b,c. Therefore, high-intensity disturbances in the forest were identified as harvest and fire due to their substantial impacts on the ecosystem, resulting in significant spectral variations in Landsat images during these events (Figure 3b). Additionally, low-intensity disturbances were categorized as insect and selective harvest, as they exhibit relatively small alterations in spectral values (Figure 3c).

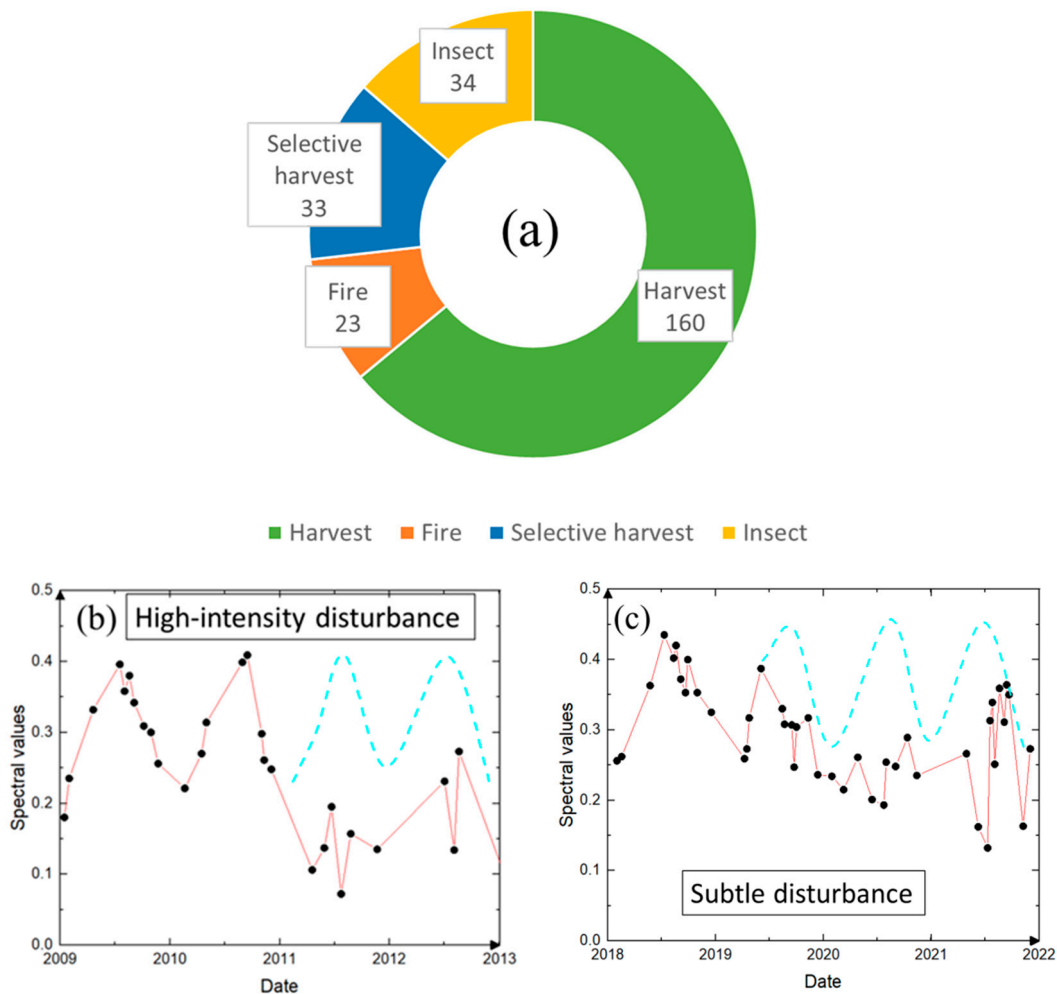


Figure 3. (a) Distribution of disturbed validation data; (b) High-intensity disturbances with significant spectral value changes, such as harvest; (c) Subtle disturbances with minor spectral value changes, such as early insect. The dashed lines in the time-series curve should illustrate a cyclic pattern, while the dotted lines indicate deviations from this regular pattern when a disturbance occurs.

3. Methods

The flowchart for detecting multi-intensity forest disturbances using the proposed AEWMA algorithm is shown in Figure 4. To adapt the AEWMA charts for Landsat data analysis, a preprocessing step is applied to the 177 acquired Landsat images. This step utilizes the harmonic regression method to mitigate the influence of seasonality. By subtracting the fitted time profiles from the observed data, both the seasonality and a significant portion of the temporal autocorrelation are effectively removed. As a result, a set of residual values is obtained, which can be assumed to follow a normal distribution and exhibit independence. These residual time series then served as the input for the AEWMA control chart, where the AEWMA value for each pixel is calculated to assess the occurrence

of disturbances. The algorithm consists of three main components: harmonic regression (Section 3.1), X-bar outlier rejection (Section 3.2), and AEWMA control chart processing (Section 3.3).

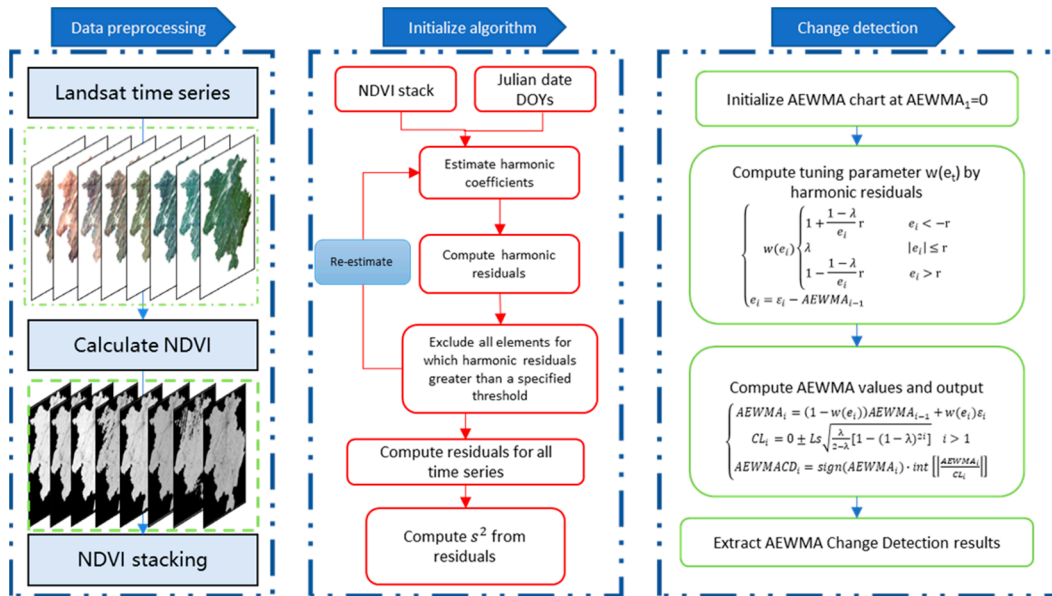


Figure 4. Flowchart of the AEWMA CD algorithm.

3.1. Harmonic Regression Model

Due to seasonal effects, this study employs harmonic regression methods to eliminate the influence of phenological variations on disturbance detection.

Given a clearly observed time series of length n , $t = [t_1, t_2, \dots, t_n]$, the following harmonic model is built during the training period:

$$y_i = a_0 + \sum_{j=1}^k \left(b_j \cos\left(\frac{2\pi j}{D} t_i\right) + c_j \sin\left(\frac{2\pi j}{D} t_i\right) \right) + \varepsilon_i \quad (1)$$

where y_i is the NDVI values, a_0 is the intercept coefficient, and k is the order of the harmonic function and set to 2, which is rooted in the observation that two harmonics suffice to represent the predominant periodic variations in the time series in the majority of cases [38]. b_j and c_j are the coefficients of the cosine and sine harmonics, respectively; ε_i is the regression residual of the Julian date; D is the number of days in a year. These model coefficients are obtained using the ordinary least-squares method.

3.2. X-Bar Outlier Rejection

After harmonic regression, the harmonic regression model may not identify clouds, shadows, or other outliers corresponding to short-term events. Introducing the Shewhart chart and utilizing the X-bar to reject outliers in a second iteration can effectively mitigate most cloud and shadow interference:

$$\hat{\beta} = (X'_{train} X_{train})^{-1} X'_{train} t_{n_{train}} \quad (2)$$

where X_{train} is a matrix composed of $n_{train} \times (1 + c_j + b_j)$ designs, and each harmonic coefficient is adjusted to the Julian date. After all elements with standardized residuals greater than a global user-specified threshold are filtered out, $\hat{\beta}$ is recalculated, and then the residuals res for the entire time series are calculated:

$$res = t - X\hat{\beta} \quad (3)$$

X is the matrix obtained by computing the full $n \times (1 + c_j + b_j)$ design, and then the training period variance s^2 is estimated:

$$s^2 = \frac{res_{n_{train}} res'_{n_{train}}}{n_{train} - 1} \quad (4)$$

where $res_{n_{train}}$ represent the residual on the training period. The first two steps were employed to eliminate seasonal changes and outliers.

3.3. AEWMACD

3.3.1. EWMACD

The EWMA values are determined as follows:

$$EWMA_i = (1 - \lambda)EWMA_{i-1} + \lambda\varepsilon_i \quad (5)$$

The initial $EWMA_1$ value of the algorithm is set to 0. λ is the smoothing coefficient, and $i = [1, 2, \dots, n]$ represents the different time steps of the time series. A value of λ close to 1 indicates that historical data are given little weight, whereas a value of λ close to 0 implies that the result of $EWMA_i$ is primarily dependent on the value of $EWMA_{i-1}$ from the previous time step.

The control limit of the EWMA chart is defined by the following equation:

$$CL_i = 0 \pm Ls\sqrt{\frac{\lambda}{2-\lambda} [1 - (1-\lambda)^{2i}]} \quad (6)$$

L is the constant of the control limits, and s is the standard deviation of all residuals during the training period. Then, the $EWMACD_i$ is calculated by dividing the $EWMA_i$ value by the CL value:

$$EWMACD_i = Sign(EWMA_i) \cdot int \left[\left| \frac{EWMA_i}{CL_i} \right| \right] \quad (7)$$

$Sign()$ is used to obtain the positive and negative sign of $EWMA_i$ value, which describes the direction of deviation from the predicted fluctuation. $\left| \frac{EWMA_i}{CL_i} \right|$ indicates the absolute value of $\frac{EWMA_i}{CL_i}$, and $int[]$ indicates the integer of this absolute value. The disturbance was signaled when the $EWMACD$ value was less than 0, and a recovery was detected when it was greater than 0. No disturbance/recovery occurs when it is equal to 0.

3.3.2. AEWMACD

EWMA charts can quickly detect small or large shifts in independent event sequences by setting different smoothing coefficients λ . However, a single EWMA control chart with a fixed λ cannot detect both large and small shifts. Brooks et al. specified a fixed smoothing coefficient of 0.3 [20]. Nevertheless, a small λ value gives less weight to the current residual, ε_i , thereby reducing the impact of high-intensity disturbances on the statistic, $EWMA_i$, which results in a significant delay effect. Capizzi and Masarotto introduced the adaptive adjustment of the smoothing coefficient function and proposed the AEWMA chart to address the aforementioned problems. The AEWMA chart has proved the feasibility of detecting both large and small shifts and is widely used [39–42].

The AEWMA chart adjusts the smoothing coefficients to an equivalent smoothing coefficient function $w(e_i)$ that can vary with the e_i at the current i moment as follows:

$$\begin{cases} w(e_i) = \begin{cases} 1 + \frac{1-\lambda}{e_i}r & e_i < -r \\ \lambda & |e_i| \leq r \\ 1 - \frac{1-\lambda}{e_i}r & e_i > r \end{cases} \\ e_i = \varepsilon_i - AEWMA_{i-1} \end{cases} \quad (8)$$

$$AEWMA_i = (1 - w(e_i))AEWMA_{i-1} + w(e_i)\varepsilon_i \quad (9)$$

where r is a threshold value that determines when to use a high smoothing coefficient or a low one. r is a constant when the chart has been designed. Low-intensity disturbances ($|e_i| \leq r$) can be detected by the cumulative amplification effect through using a small equivalent smoothing coefficient; Conversely, when a high-intensity disturbance agent occurred ($e_i < -r$ or $e_i > r$), the equivalent smoothing coefficient $w(e_i)$ adaptively obtain larger and more weight was assigned to current residual ε_i with high negative value and then the sudden drop of current chart value $AEWMA_i$ makes the high-intensity disturbance quickly detected, effectively overcoming the temporal delay problem.

The $AEWMACD_i$ is then calculated by dividing the $AEWMA_i$ value by the CL value:

$$AEWMACD_i = \text{sign}(AEWMA_i) \cdot \text{int} \left[\left| \frac{AEWMA_i}{CL_i} \right| \right] \quad (10)$$

The control limit is the same as $EWMACD$ in Equation (6). When the $AEWMACD$ value consecutively exceeds the control limit three times, a forest pixel is marked as disturbed, and no disturbance occurs if its $AEWMACD$ value is equal to 0. The value of λ in Equation (6) was determined through experimental testing by repeatedly executing the $AEWMA$ chart on a representative subset of this study. The initial value of $AEWMA_1$ is set to 0, and the value of the constant L is set to 3 based on experience [38].

3.3.3. Parameter Optimization

While the $AEWMACD$ algorithm dynamically adjusts the smoothing coefficient, it is important to define the initial value of the smoothing coefficient. Upon observing the composite image, the initial smoothing coefficient struggles to detect these disturbances when it is set to high values, such as 0.3 or 0.4, as shown in Figure 5e,f. Thus, we initially set λ to 0.15 as our smoothing coefficient. The experiments, depicted in Figure 6, revealed that $r > 0.15$ resulted in poor aggregation of disturbance patches. Therefore, the effective threshold value r was set to 0.1 for achieving multi-intensity forest disturbance detection.

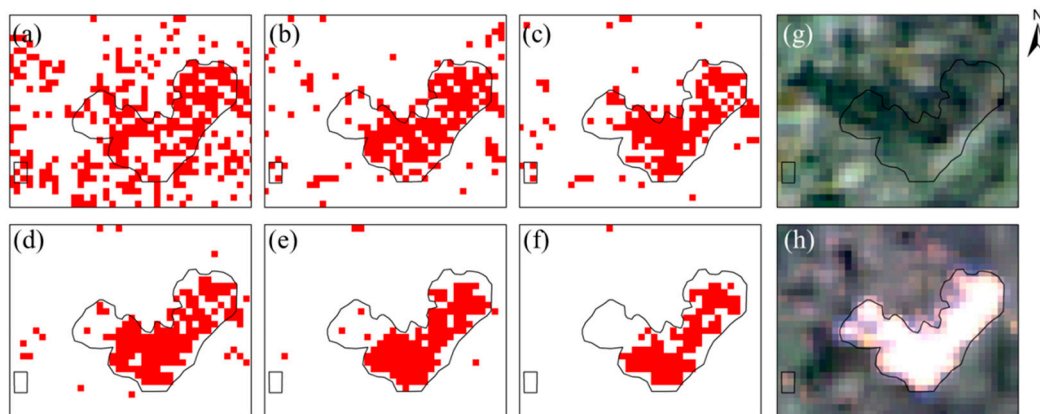


Figure 5. AEWMACD change detection results with different λ (the black lines represent the disturbance area by manual interpretation): (a) $\lambda = 0.05$; (b) $\lambda = 0.1$; (c) $\lambda = 0.15$; (d) $\lambda = 0.2$; (e) $\lambda = 0.3$; (f) $\lambda = 0.4$; (g) Landsat image on 21 January 2014; (h) Landsat image on 8 June 2014.

3.4. Accuracy Assessment

An accuracy assessment was performed, covering both spatial and temporal dimensions. For the spatial accuracy assessment, a visual comparison were conducted between reference data and detected disturbances. The locations where disturbances matched the reference data were meticulously marked, and essential metrics were then quantified, including Overall Accuracy (OA), User's Accuracy (UA), Producer's Accuracy (PA), and Kappa value. In the temporal accuracy assessment approach, the date corresponding to the

first image in which disturbance was identified through visual interpretation was treated as the initial occurrence date of disturbance.

$$Kappa = \frac{p_0 - p_e}{1 - p_e} \quad (11)$$

p_0 is the observed agreement, representing the proportion of agreement actually observed. p_e is the expected agreement, representing the agreement expected to occur by chance.

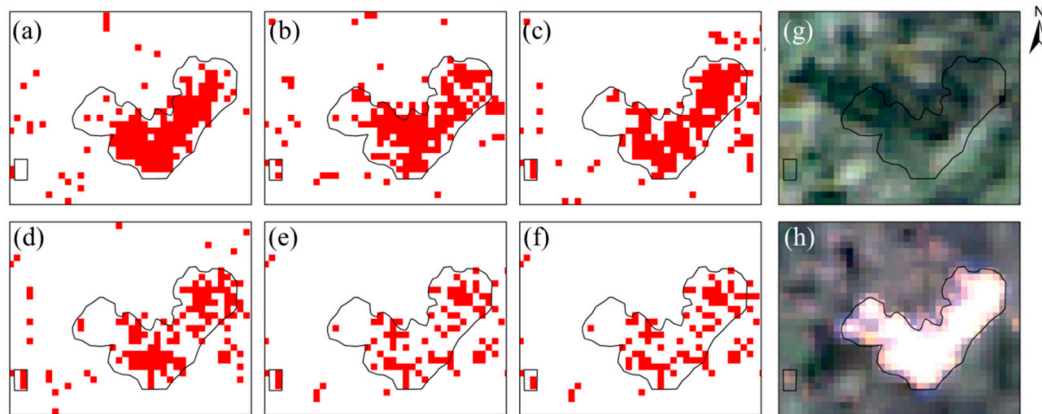


Figure 6. AEWMACD change detection results with different r (the black lines represent the disturbance area by manual interpretation): (a) $r = 0.05$; (b) $r = 0.1$; (c) $r = 0.15$; (d) $r = 0.2$; (e) $r = 0.3$; (f) $r = 0.4$; (g) Landsat image on 21 January 2014; (h) Landsat image on 8 June 2014.

4. Results

The algorithm generates a stacked raster as output, where each layer corresponds to a disturbance period based on the Landsat NDVI date in the stack. We demonstrate the algorithm's feasibility of detecting multi-intensity forest disturbances (Section 4.1) and assess its accuracy (Section 4.2). The results for the entire study area of AEWMACD and EWMACD are depicted in Figure 7.

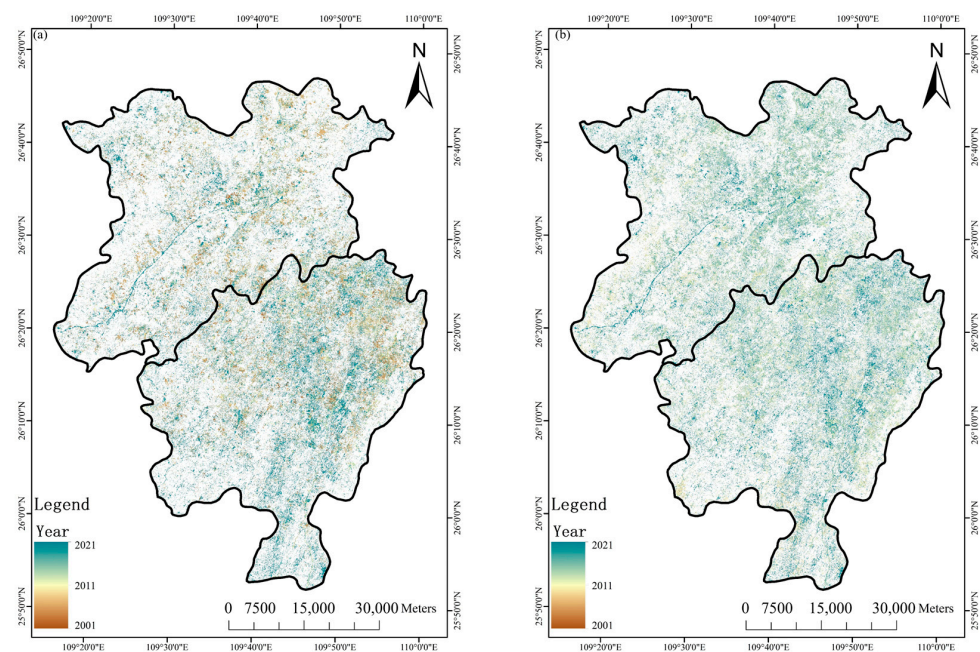


Figure 7. (a) First occurrence of disturbances in the detection results of AEWMACD; and (b) First occurrence of disturbances in the detection results of EWMACD.

4.1. Feasibility Analysis of Detecting Multi-Intensity Disturbances Using the AEWMACD Algorithm

4.1.1. Low-Intensity Forest Disturbance Detection

The AEWMACD algorithm incorporates a low smoothing coefficient, enabling it to effectively identify low-intensity disturbances such as insect damage and selective harvesting. As illustrated in Figure 8, an insect agent occurred on 26 November 2007 (Figure 8b,d). The AEWMACD values of the disturbed forest pixel showed that the insect agent was accurately and timely detected at the initial disturbance date (the dashed line in Figure 8e). Furthermore, an example of detecting selective harvesting is shown in Figure 9. Although harvesting only occurred on part of the forest pixel, the algorithm still successfully detected the disturbed pixel. This demonstration underscores our adaptive algorithm's ability to identify low-intensity disturbances, highlighting the strengths inherited from the EWMACD algorithm.

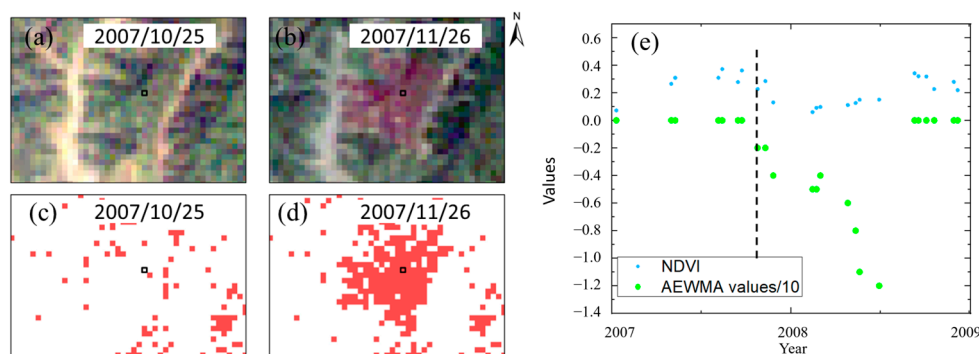


Figure 8. Low-intensity disturbance caused by insects: (a,b) depict Landsat images in different periods; (c,d) illustrate the AEWMACD change detection results in different periods; and (e) presents the NDVI and AEWMA values within the black box in the images, and the dashed line marks the moment of disturbance occurrence.

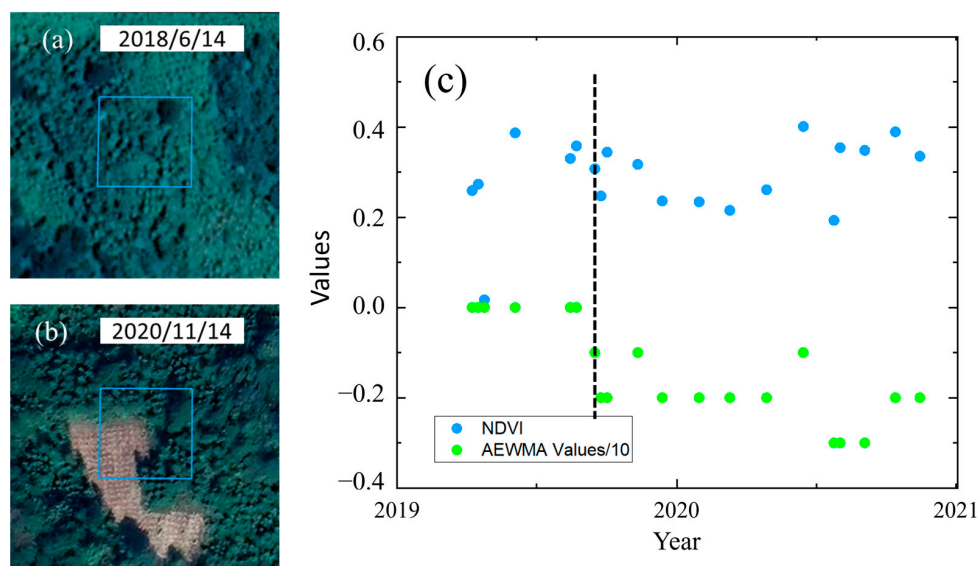


Figure 9. Low-intensity disturbance caused by selective harvest: (a,b) show the high-resolution images from Google Earth PRO; and (c) denotes NDVI and AEWMA values in the blue box (a pixel in the Landsat image), and the dashed line represents the moment when the disturbance occurred.

4.1.2. High-Intensity Forest Disturbance Detection

To assess the effectiveness of the AEWMACD algorithm in responding to high-intensity disturbances, a forest patch where a harvest event occurred on 4 December

2010 was selected as an illustrative case (Figure 10). While the EWMACD algorithm failed to promptly identify the disturbance in the green box on the initial disturbance date (Figure 10h), the AEWMACD, featuring adaptively adjusted smoothing coefficients, successfully detected this disturbance in a timely manner (Figure 10e). It showed that the EWMACD algorithm identified the disturbance with a one-time step delay, but the AEWMACD algorithm detected the disturbance promptly as it occurred (Figure 10j). Additionally, a fire took place on 10 November 2007, as illustrated in Figure 11. Through adaptively adjusting the smoothing coefficient, the AEWMACD algorithm with an increased smoothing coefficient can timely and effectively detect the fire agent (Figure 11j). A comparison of the algorithm's detection results with the actual situation revealed the high responsiveness of the AEWMACD algorithm to high-intensity disturbances.

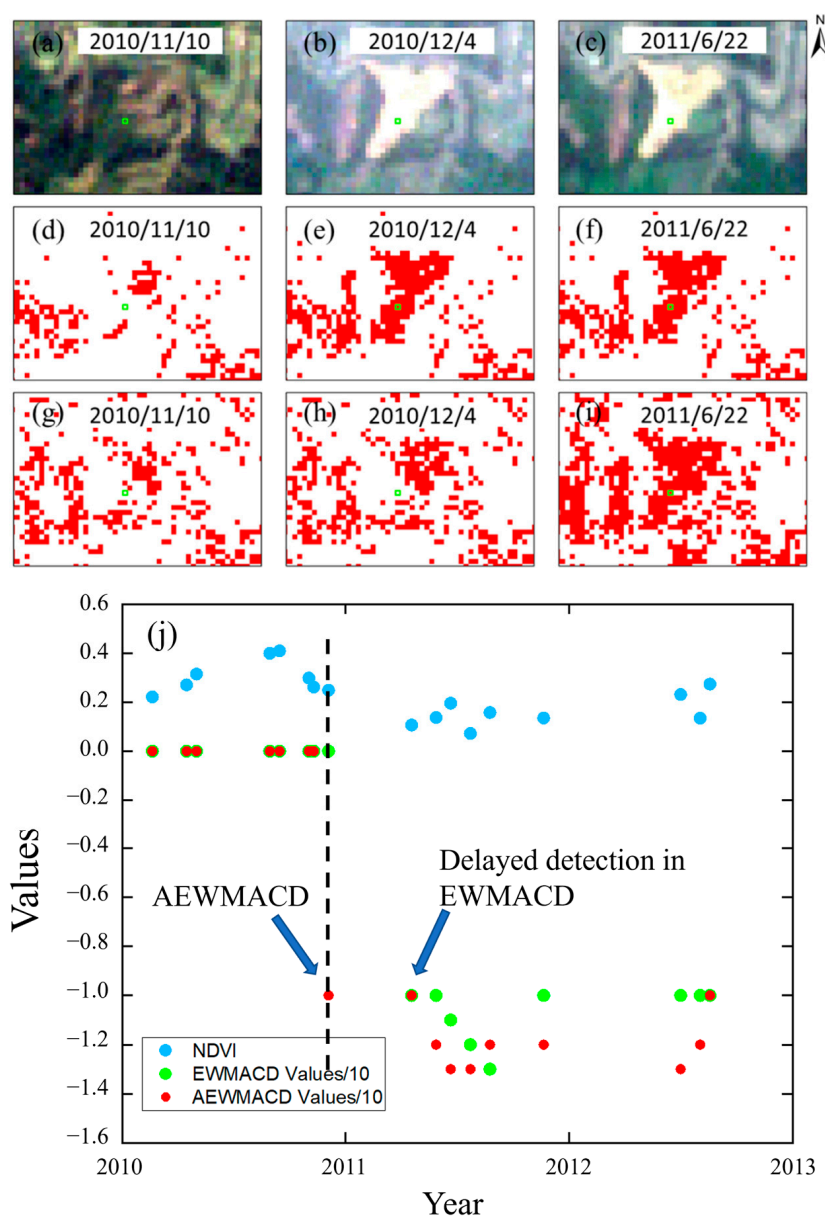


Figure 10. High-intensity disturbances caused by harvest and the delayed detection problem addressed by EWMACD were corrected by AEWMACD: (a–c) represent the Landsat images in different periods; (d–f) represent the AEWMACD change detection results in different periods; (g–i) represent the EWMACD change detection results in different periods; and (j) represent the NDVI, EWMACD, and AEWMACD values of the pixel in the green box, and the black dashed line represents the time that disturbance occurred.

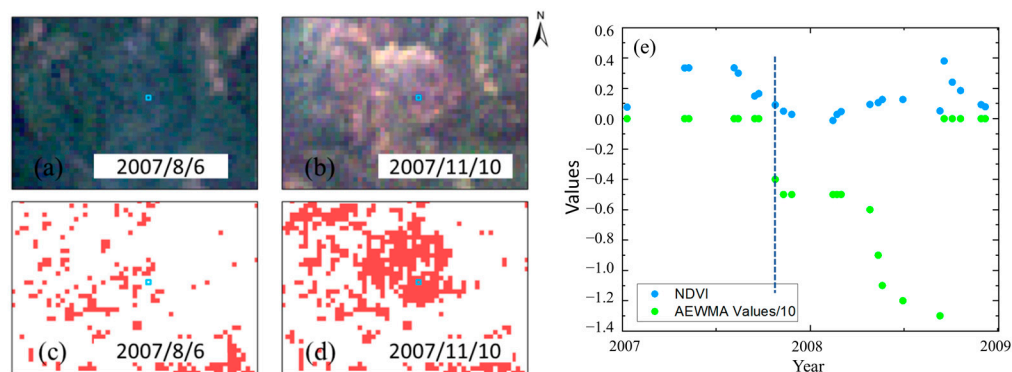


Figure 11. High-intensity disturbance caused by fire: (a,b) represent the Landsat images before and after the fire, respectively; (c,d) represent the AEWMACD change detection results in different periods; and (e) represents the NDVI and AEWMA values in the blue box, and the dashed line represents the moment when the disturbance occurred.

4.1.3. Multi-Intensity Forest Disturbance Detection

The improved AEWMACD algorithm exhibits robust detection performance for both low-intensity and high-intensity disturbances, as demonstrated in the example above. Landsat's extensive time series data, with long archival periods covering regions susceptible to multi-intensity disturbances, is well-suited for simultaneous detection of pixels affected by various disturbance levels. To illustrate this capability, we examine a specific pixel (Figure 12, indicated by the black box) experiencing both high- and low-intensity disturbances at different periods. Initially, a low-intensity disturbance, signifying an insect, was detected from 6 August 2007 to 10 November 2007 (Figure 12a,b). Subsequently, following stabilization and model retraining, a high-intensity disturbance was identified from 24 July 2020 to 12 December 2020 (Figure 12d,e). This pixel's multiple disturbances highlight the AEWMACD method's ability to detect multi-intensity disturbances within the same pixel at different periods.

4.2. Assessment of Disturbance Detection Accuracy

4.2.1. Assessment of Disturbance Detection Accuracy in the Spatial Domain

The validation data were used to assess the AEWMACD algorithm. Table 2 provides a comparison of spatial accuracy between the EWMACD and AEWMACD algorithms, and they reveal superior performance by the AEWMACD algorithm with an accuracy of 85.2%. The Kappa value for AEWMACD is 0.70, whereas for EWMACD, it is 0.52. Notably, for disturbed samples, the user accuracy and producer accuracy were separately 86.1% and 84%, while stable samples exhibited a user accuracy of 84.4% and a producer accuracy of 86.4%. Furthermore, we conducted accuracy assessments for detecting various types of disturbances (Table 3). The results showed that the AEWMACD algorithm achieved an accuracy of 84.4% for detecting harvest disturbances, 79.2% for fire detection, 82.4% for insect disturbances, and 87.5% for selective harvest disturbances. The adaptive approach outperformed the EWMACD algorithm, especially in cases of high-intensity disturbances such as harvest and fire. Additionally, in low-intensity cases, the accuracy of both algorithms was comparable.

The commission errors are primarily attributed to two factors: (1) continuous noise or cloud interference and (2) mountain shadows. (1) In the algorithm fitting process, we utilize the Shewhart chart for outlier rejection, effectively eliminating most instances of cloud interference. However, some residual thin cloud pixels that escape Shewhart chart filtering can still be erroneously identified as disturbances, as illustrated in Figure 13. Notably, the majority of the pixels in the blue box in Figure 13b–d remain obscured by continuous clouds for three consecutive periods, resulting in certain pixels being incorrectly flagged as disturbances on 3 August 2012 (Figure 13f). (2) As satellites capture images during Earth's

orbit, the acquired data may not be in orthorectified form. Moreover, different capture times can also result in shadows affecting the images. As illustrated in Figure 14, the pixels within the red box consistently represent forested areas. However, the influence of shadows causes variations in NDVI values. These subtle spectral changes occur continuously for more than three times, leading the algorithm to detect them as low-intensity disturbances. Therefore, the algorithm may exhibit commission errors in areas covered by mountain shadows.

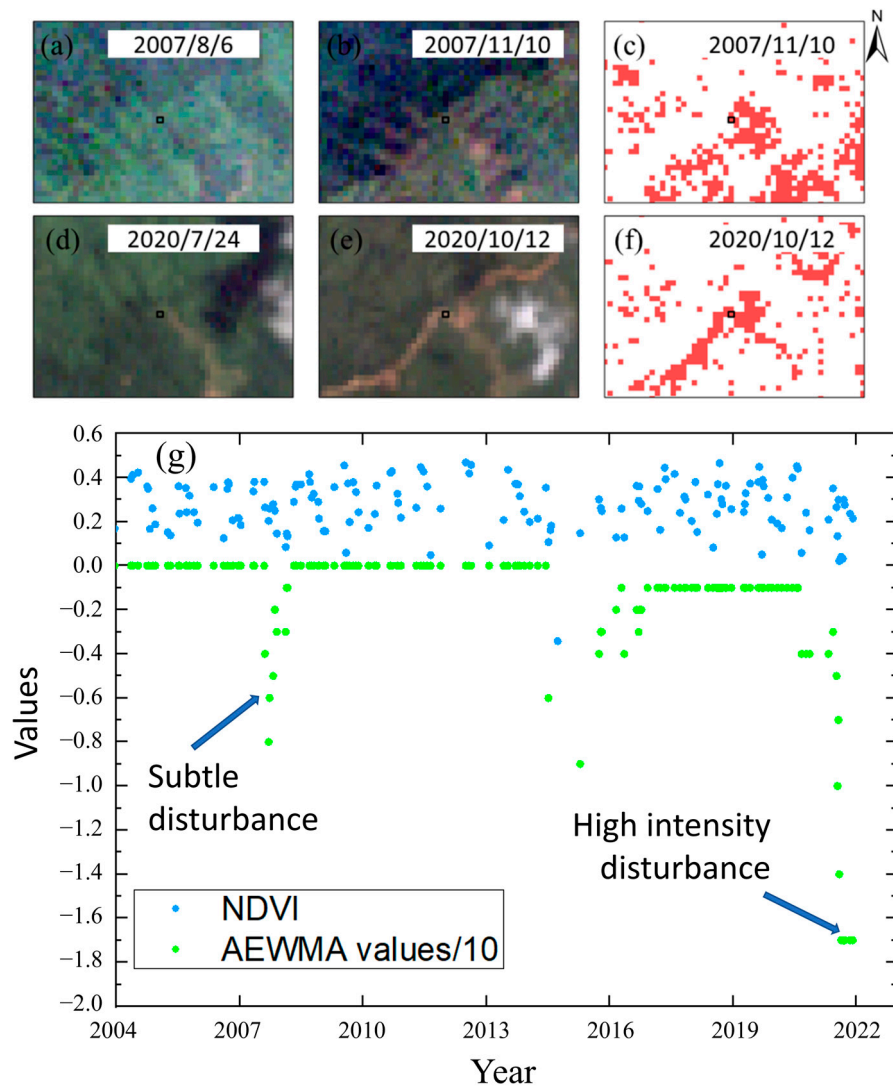


Figure 12. Disturbance of different intensities by insect and harvest: (a,b,d,e) represent the Landsat images in different periods; (c) represents the AEWMACD change detection results of subtle disturbance; (f) represents the change detection results of high-magnitude disturbance; and (g) represents the NDVI and AEWMA values of the pixel in the black box.

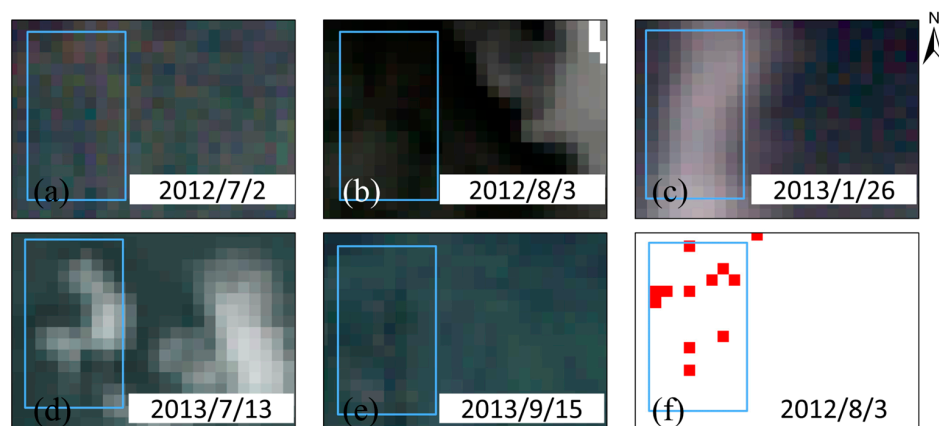
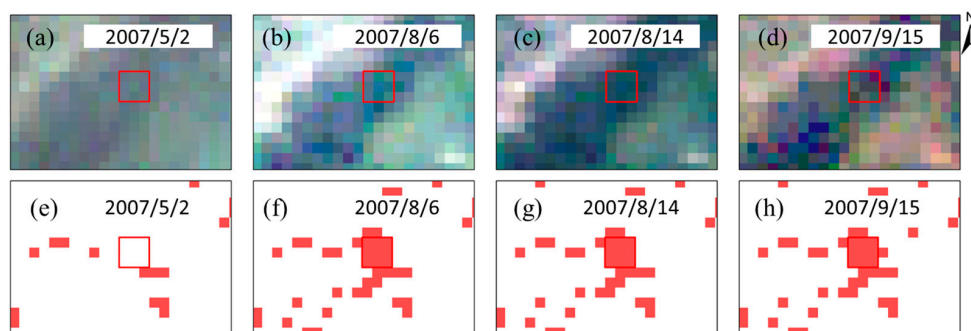
Table 2. Spatial accuracy assessment of AEWMACD and EWMACD results.

Result \ Sample	AEWMACD				EWMACD			
	Disturbance	No Disturbance	Total	UA ¹	Disturbance	No Disturbance	Total	UA ¹
Disturbance	210	34	244	84.0%	183	53	236	77.5%
No disturbance	40	216	256	86.4%	67	197	264	74.6%
total	250	250	500		250	250	500	
PA ²	84.0%	86.4%	OA ³	85.2%	73.2%	78.8%	OA ³	76.0%
			Kappa	0.70			Kappa	0.52

¹ UA represents the User’s accuracy. ² PA represents the Producer’s accuracy. ³ OA represents overall accuracy.

Table 3. Spatial accuracy assessment of EWMACD results.

Types	AEWMACD			EWMACD		
	Disturbance	No Disturbance	Producer's Accuracy	Disturbance	No Disturbance	Producer's Accuracy
Harvest (high)	135	25	84.4%	114	46	71.3%
Fire (high)	18	5	79.2%	14	10	58.3%
Insect (low)	28	5	82.4%	27	7	79.4%
Selective harvest (low)	28	4	87.5%	28	4	87.5%

**Figure 13.** Commission errors caused by thin clouds or cloud shadows in the blue box, which represents some pixels in this region were detected as disturbances: (a–e) represent the Landsat images in different periods; (f) represents the AEWMACD change detection results on 3 August 2012.**Figure 14.** Commission error caused by mountain shadows in the red box, which represents all pixels in this region were detected as disturbances: (a–d) represent the Landsat images in different periods; (e–h) represent the AEWMACD change detection results in different periods.

The main reasons for omission errors are twofold: (1) extreme small changes in the NDVI values of the pixels when the disturbance occurs, and (2) the absence of multiple available clear observations during the disturbance. (1) The primary reason lies in the minimal change in NDVI values, resulting in smaller residual values after harmonic regression. As shown in Figure 15, it was indicating disturbances on 19 April 2011 in this region. However, the NDVI value only changed from 0.268 to 0.141. The minimal change in NDVI values led to the omission error, and due to the rounding down of values for noise reduction in the images, the subtle changes were not detected as disturbances (red box in Figure 15). (2) Another contributing factor is the limited availability of Landsat imagery during the disturbance event, which failed to meet the minimum requirement of three steps. The Landsat images contained less than 60% contaminated pixels, which meant that some areas lacked sufficient available images. As shown in Figure 16, only two

clear observations in this region visually displayed disturbances. Since this number did not meet the requirement of three consecutive observations, the disturbance was not detected.

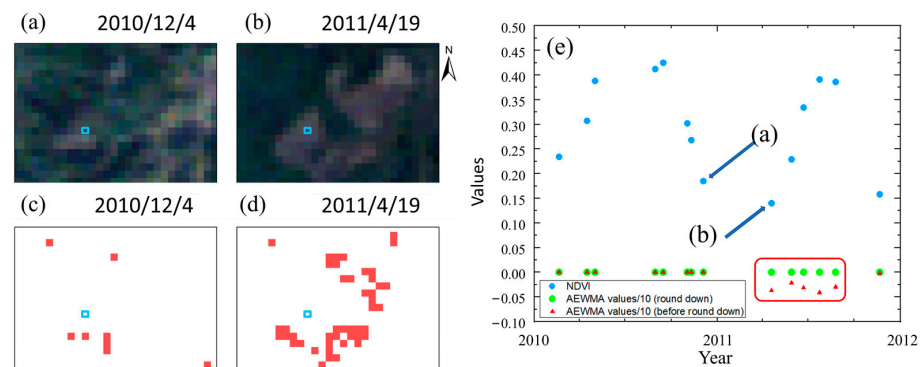


Figure 15. Omission error due to small change in value: (a,b) represent the Landsat images in different periods; (c,d) represent the AEWMA change detection results in different periods; and (e) represent the NDVI, AEWMA, and AEWMA values of the pixel that have not been rounded in the blue box and the red box represents the difference in AEWMA values before and after round down.

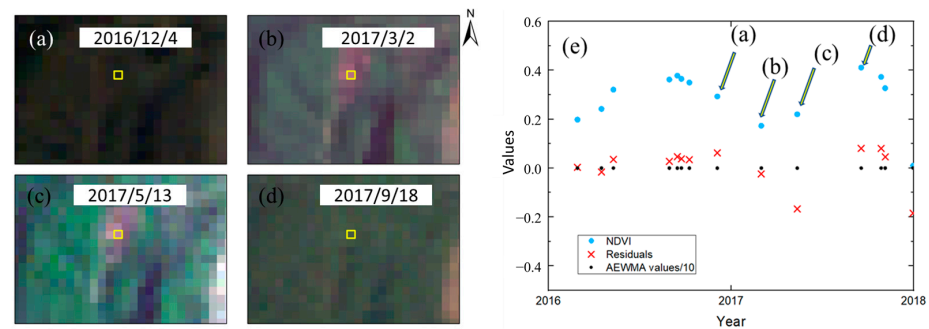


Figure 16. Omission error due to insufficient three clear observations: (a–d) represent the Landsat images in different periods; and (e) represent the NDVI and AEWMA values of the pixel in the yellow box.

4.2.2. Assessment of Disturbance Detection Accuracy in the Temporal Domain

The date of forest disturbance occurrences was determined by identifying the date corresponding to the first image through manual visual interpretation. This approach was applied uniformly, regardless of whether it indicated complete or partial disturbances as identified through manual visual interpretation. The introduction of the adaptive function led to a substantial improvement in the algorithm's temporal accuracy compared with the EWMACD algorithm (Table 4), allowing for more precise detection of disturbances. To tackle the delay effect associated with high-intensity disturbances, we heightened the algorithm's sensitivity by adaptively increasing the smoothing coefficient. The accuracy of the algorithm's temporal detection was validated using spatially accurately detected samples. Manual verification of these samples confirmed the algorithm's proficiency in detecting disturbances, resulting in an overall temporal accuracy of 96.7% (89.1% + 7.6%) if one time step delay (late = 1 time step) in detecting disturbance is acceptable. In contrast, the EWMACD algorithm achieved a temporal accuracy of 87.1% (73.3% + 13.8%).

Similar to the analysis of spatial accuracy, the temporal accuracy of different disturbance types was also assessed (Table 5). The accuracy of AEWMA CD was 95.6% (87.4% + 8.2%) for harvest and 94.7% (89.4% + 5.3%) for fire, which means AEWMA CD achieved high temporal accuracy for high-intensity disturbances. Additionally, the AEWMA CD demonstrated a significant reduction in delay effects compared to the EWMACD, especially in the context of high-intensity disturbances. Meanwhile, both of the algorithms exhibit similar temporal accuracy for low-intensity disturbance detection.

Table 4. Temporal accuracy assessment results.

	Same Time Step	Late = 1 Time Step	Late ≥ 2 Time Steps	Total
AEWAMACD Disturbance	187	16	7	210
AEWAMACD Proportion	89.1%	7.6%	3.3%	100%
EWMACD Disturbance	154	29	27	210
EWMACD Proportion	73.3%	13.8%	12.9%	100%

Table 5. Temporal accuracy assessment of different disturbance types.

	Types	Same Time Step	Late = 1 Time Step	Late ≥ 2 Time Steps	Total
AEWAMACD Proportion	Harvest (high)	118 (87.4%)	11 (8.2%)	6 (4.4%)	135
	Fire (high)	17 (89.4%)	1 (5.3%)	1 (5.3%)	19
	Insect (low)	28 (100.0%)	0 (0.0%)	0 (0.0%)	28
	Selective harvest(low)	24 (85.7%)	4 (14.3%)	0 (0.0%)	28
EWAMACD Proportion	Harvest (high)	92 (68.2%)	21 (15.5%)	22 (16.3%)	135
	Fire (high)	12 (63.2%)	3 (15.8%)	4 (21.0%)	19
	Insect (low)	26 (92.9%)	2 (7.14%)	0 (0.00%)	28
	Selective harvest(low)	24 (85.7%)	3 (10.7%)	1 (3.6%)	28

Although there have been significant improvements in time accuracy, addressing the delay effect remains a challenge. As shown in Figure 17, while forest pixels experienced disturbances on 19 April 2011, changes were observed in individual pixels (the blue box) during the subsequent period on 29 May 2011, indicating a one-time step delay. This delay may be attributed to the inadequate fit of the harmonic model, causing disturbances that did not exceed the control limits when they occurred.

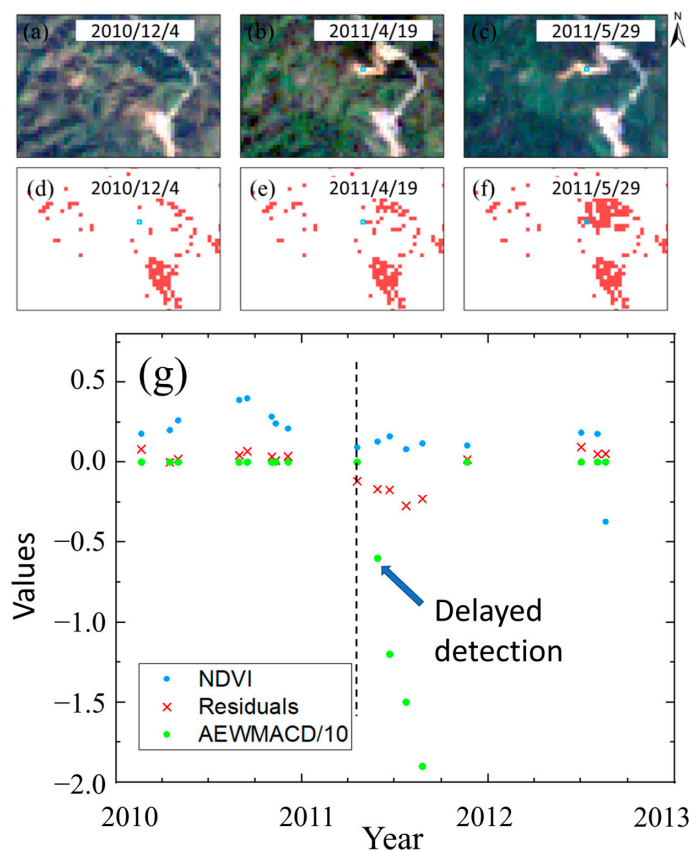


Figure 17. Delayed detection problem by the seasonal change: (a–c) represent the Landsat images in different periods; (d–f) represent the AEWAMACD change detection results in different periods; and (g) represent the NDVI values, residuals, AEWMA values, and signed disturbance values of the pixel in the blue box, and the dashed line represents the moment when the disturbance occurred.

5. Discussion

The AEWMACD algorithm achieves the detection of multiple forest disturbances coexisting. Compared to EWMACD, AEWMACD reduces time delays in detecting high-intensity disturbances. In contrast to algorithms primarily designed for high-intensity disturbances, AEWMACD exhibits higher sensitivity to low-intensity disturbances.

The method also exhibits geographical limitations. The study area is primarily characterized by evergreen tree species. When applying this method to regions with a diverse array of tree species, its applicability remains to be validated. Moreover, if extending the AEWMACD to tropical regions, the frequent influence of clouds and rainfall leads to sparse availability of usable images, posing challenges to meeting the requirements of harmonic regression [43] and thus affecting the feasibility of the algorithm.

The AEWMACD algorithm utilizes a single-band feature as its input. As noted by Brooks et al. [20,32], relying on a single feature may result in greater errors compared to the use of multiple features. This is because some features exhibit higher sensitivity to specific disturbances. For instance, the Normalized Burn Ratio (NBR) offers significant advantages in forest fire and harvest detection as it yields values greater than those resulting from road construction and insect activity [44]. Additionally, in the case of harvest, the Shortwave Infrared 1 (SWIR1) band tends to display higher values than those following a fire [45]. Algorithms that incorporate multiple features or Landsat image bands tend to achieve higher detection accuracy, as exemplified by CCDC and COLD. Additionally, scholars have introduced the MAEWMA chart [46] as an extension of the MEWMA chart [47] and AEWMA chart, demonstrating superior results in quality control processes [48–51]. The MAEWMA chart utilizes multidimensional features for quality control detection, providing a new approach to incorporating spectral, temporal, and spatial characteristics into change detection algorithms. The pursuit of this multi-feature-based approach holds potential for future research.

During our experiments, we encountered another issue concerning the influence of image quality on detection accuracy. Specifically, regions with continuous thin cloud shadows could be erroneously identified as disturbances. Although the Shewhart X-bar chart can help to eliminate outliers caused by clouds or shadows, it does not entirely eliminate errors, as shown in Figure 12. This will be explored in our future research. Furthermore, some pixel values may not exceed the control limits, primarily due to minor spectral variations, which could potentially lead to omission errors. However, neighboring pixels may exhibit more significant differences and be correctly identified as disturbances. To mitigate this concern, we intend to incorporate an object-based change detection method [52] to filter out these omission errors, ensuring the completeness of detected patches within the same region [53].

Additionally, the detection algorithm only detected forest disturbances and did not differentiate between disturbance types. This limitation restricts their utility for forest resource management. Therefore, in future research, we intend to integrate classification algorithms into the change detection process to attribute various intensities of disturbances.

6. Conclusions

In this study, we proposed an online change detection algorithm known as AEWMACD for detecting forest disturbances with different intensities. EWMACD algorithms determine changes using fixed smoothing coefficients, which poses challenges when both high- and low-intensity disturbances occur. To address the limitation, the proposed AEWMACD algorithm can adaptively adjust smoothing coefficients to enhance its effectiveness in multi-intensity disturbance detection. It showed a rapid response of the AEWMACD algorithm to high-intensity disturbances, and the sensitivity to low-intensity disturbances proved the potentiality of the algorithm for early warning. The proposed AEWMACD algorithm presents an alternative for quickly and accurately capturing diverse forest disturbance agents driven by natural causes and human activities, laying the foundation for subsequent attribution of forest disturbance agents. In future endeavors, the emphasis will

be on optimizing the method for regions characterized by diverse tree species, with the goal of achieving broader applications. Additionally, further research will be conducted to address challenges related to multiple features, object-based approaches, and the classification of disturbance types.

Author Contributions: Conceptualization, T.Z., L.W., X.L., M.L. and C.C.; methodology, T.Z. and L.W.; software, T.Z.; validation, T.Z., B.Y., Y.X. and S.Z.; formal analysis, T.Z. and L.W.; data curation, T.Z., B.Y., Y.X. and S.Z.; writing—original draft preparation, T.Z.; writing—review and editing, T.Z., L.W., X.L., M.L. and C.C.; funding acquisition, L.W. All authors have read and agreed to the published version of the manuscript.

Funding: This research was funded by the National Natural Science Foundation of China, grant number 41701387.

Data Availability Statement: The data presented in this study are available on request from the corresponding author.

Acknowledgments: The authors express their gratitude to the USGS for providing Landsat data and to Brooks for generously sharing the R codes of the EWMACD algorithm.

Conflicts of Interest: The authors declare no conflict of interest. The funding sponsors had no role in the design of this study, in the collection, analysis, or interpretation of data, in the writing of this manuscript, or in the decision to publish this results.

References

- Hansen, M.C.; Loveland, T.R. A review of large area monitoring of land cover change using Landsat data. *Remote Sens. Environ.* **2012**, *122*, 66–74. [[CrossRef](#)]
- Barlow, J.; Lennox, G.D.; Ferreira, J.; Berenguer, E.; Lees, A.C.; Mac Nally, R.; Thomson, J.R.; Ferraz, S.F.D.; Louzada, J.; Oliveira, V.H.F.; et al. Anthropogenic disturbance in tropical forests can double biodiversity loss from deforestation. *Nature* **2016**, *535*, 144–147. [[CrossRef](#)] [[PubMed](#)]
- Coop, J.D.; Parks, S.A.; Stevens-Rumann, C.S.; Crausbay, S.D.; Higuera, P.E.; Hurteau, M.D.; Tepley, A.; Whitman, E.; Assal, T.; Collins, B.M.; et al. Wildfire-Driven Forest Conversion in Western North American Landscapes. *Bioscience* **2020**, *70*, 659–673. [[CrossRef](#)] [[PubMed](#)]
- Seidl, R.; Thom, D.; Kautz, M.; Martin-Benito, D.; Peltoniemi, M.; Vacchiano, G.; Wild, J.; Ascoli, D.; Petr, M.; Honkaniemi, J.; et al. Forest disturbances under climate change. *Nat. Clim. Chang.* **2017**, *7*, 395–402. [[CrossRef](#)] [[PubMed](#)]
- Bullock, E.L.; Woodcock, C.E.; Souza, C.; Olofsson, P. Satellite-based estimates reveal widespread forest degradation in the Amazon. *Glob. Chang. Biol.* **2020**, *26*, 2956–2969. [[CrossRef](#)] [[PubMed](#)]
- Liu, W.; Wang, X.; Lu, F.; Ouyang, Z. Influence of afforestation, reforestation, forest logging, climate change, CO₂ concentration rise, fire, and insects on the carbon sequestration capacity of the forest ecosystem. *Acta Ecol. Sin.* **2016**, *36*, 2113–2122.
- Thom, D.; Seidl, R. Natural disturbance impacts on ecosystem services and biodiversity in temperate and boreal forests. *Biol. Rev.* **2016**, *91*, 760–781. [[CrossRef](#)] [[PubMed](#)]
- Feng, Y.; Ziegler, A.D.; Elsen, P.R.; Liu, Y.; He, X.Y.; Spracklen, D.V.; Holden, J.; Jiang, X.; Zheng, C.M.; Zeng, Z.Z. Upward expansion and acceleration of forest clearance in the mountains of Southeast Asia. *Nat. Sustain.* **2021**, *4*, 892–899. [[CrossRef](#)]
- Oeser, J.; Heurich, M.; Senf, C.; Pflugmacher, D.; Kuemmerle, T. Satellite-based habitat monitoring reveals long-term dynamics of deer habitat in response to forest disturbances. *Ecol. Appl.* **2021**, *31*, 1–12. [[CrossRef](#)]
- Schneider, A. Monitoring land cover change in urban and pen-urban areas using dense time stacks of Landsat satellite data and a data mining approach. *Remote Sens. Environ.* **2012**, *124*, 689–704. [[CrossRef](#)]
- Woodcock, C.E.; Allen, R.; Anderson, M.; Belward, A.; Bindschadler, R.; Cohen, W.; Gao, F.; Goward, S.N.; Helder, D.; Helmer, E.; et al. Free access to Landsat imagery. *Science* **2008**, *320*, 1011. [[CrossRef](#)] [[PubMed](#)]
- Banskota, A.; Kayastha, N.; Falkowski, M.J.; Wulder, M.A.; Froese, R.E.; White, J.C. Forest Monitoring Using Landsat Time Series Data: A Review. *Can. J. Remote Sens.* **2014**, *40*, 362–384. [[CrossRef](#)]
- Seidl, R.; Schelhaas, M.J.; Rammer, W.; Verkerk, P.J. Increasing forest disturbances in Europe and their impact on carbon storage. *Nat. Clim. Chang.* **2014**, *4*, 806–810. [[CrossRef](#)] [[PubMed](#)]
- Griffiths, P.; Kuemmerle, T.; Baumann, M.; Radeloff, V.C.; Abrudan, I.V.; Lieskovsky, J.; Munteanu, C.; Ostapowicz, K.; Hostert, P. Forest disturbances, forest recovery, and changes in forest types across the Carpathian ecoregion from 1985 to 2010 based on Landsat image composites. *Remote Sens. Environ.* **2014**, *151*, 72–88. [[CrossRef](#)]
- Singh, A. Digital change detection techniques using remotely-sensed data. *Int. J. Remote Sens.* **1989**, *10*, 989–1003. [[CrossRef](#)]
- Kennedy, R.E.; Yang, Z.G.; Cohen, W.B. Detecting trends in forest disturbance and recovery using yearly Landsat time series: 1. LandTrendr—Temporal segmentation algorithms. *Remote Sens. Environ.* **2010**, *114*, 2897–2910. [[CrossRef](#)]

17. Verbesselt, J.; Hyndman, R.; Newnham, G.; Culvenor, D. Detecting trend and seasonal changes in satellite image time series. *Remote Sens. Environ.* **2010**, *114*, 106–115. [[CrossRef](#)]
18. Zhu, Z.; Woodcock, C.E. Continuous change detection and classification of land cover using all available Landsat data. *Remote Sens. Environ.* **2014**, *144*, 152–171. [[CrossRef](#)]
19. Yang, B.W.; Wu, L.; Ju, Z.S.; Liu, X.N.; Liu, M.L.; Zhang, T.W.; Xu, Y.Q. Sub-Annual Scale LandTrendr: Sub-Annual Scale Deforestation Detection Algorithm Using Multi-Source Time Series Data. *IEEE J. Sel. Top. Appl. Earth Obs. Remote Sens.* **2023**, *16*, 8563–8576. [[CrossRef](#)]
20. Brooks, E.B.; Wynne, R.H.; Thomas, V.A.; Blinn, C.E.; Coulston, J.W. On-the-Fly Massively Multitemporal Change Detection Using Statistical Quality Control Charts and Landsat Data. *IEEE Trans. Geosci. Remote Sens.* **2014**, *52*, 3316–3332. [[CrossRef](#)]
21. Wu, L.; Li, Z.L.; Liu, X.N.; Zhu, L.H.; Tang, Y.B.; Zhang, B.Y.; Xu, B.L.; Liu, M.L.; Meng, Y.Y.; Liu, B.Y. Multi-Type Forest Change Detection Using BFAST and Monthly Landsat Time Series for Monitoring Spatiotemporal Dynamics of Forests in Subtropical Wetland. *Remote Sens.* **2020**, *12*, 341. [[CrossRef](#)]
22. Hethcoat, M.G.; Carreiras, J.M.B.; Edwards, D.P.; Bryant, R.G.; Quegan, S. Detecting tropical selective logging with C-band SAR data may require a time series approach. *Remote Sens. Environ.* **2021**, *259*, 11. [[CrossRef](#)]
23. Watts, L.M.; Laffan, S.W. Effectiveness of the BFAST algorithm for detecting vegetation response patterns in a semi-arid region. *Remote Sens. Environ.* **2014**, *154*, 234–245. [[CrossRef](#)]
24. Katagis, T.; Gitas, I.Z.; Toukiloglou, P.; Veraverbeke, S.; Goossens, R. Trend analysis of medium- and coarse-resolution time series image data for burned area mapping in a Mediterranean ecosystem. *Int. J. Wildland Fire* **2014**, *23*, 668–677. [[CrossRef](#)]
25. Esteban, J.; Fernández-Landa, A.; Tomé, J.L.; Gómez, C.; Marchamalo, M. Identification of Silvicultural Practices in Mediterranean Forests Integrating Landsat Time Series and a Single Coverage of ALS Data. *Remote Sens.* **2021**, *13*, 3611. [[CrossRef](#)]
26. Zhu, Z.; Woodcock, C.E. Object-based cloud and cloud shadow detection in Landsat imagery. *Remote Sens. Environ.* **2012**, *118*, 83–94. [[CrossRef](#)]
27. Zhu, Z.; Zhang, J.X.; Yang, Z.Q.; Aljaddani, A.H.; Cohen, W.B.; Qiu, S.; Zhou, C.L. Continuous monitoring of land disturbance based on Landsat time series. *Remote Sens. Environ.* **2020**, *238*, 111116. [[CrossRef](#)]
28. Saxena, R.; Watson, L.T.; Wynne, R.H.; Brooks, E.B.; Thomas, V.A.; Yang, Z.Q.; Kennedy, R.E. Towards a polyalgorithm for land use change detection. *ISPRS J. Photogramm. Remote Sens.* **2018**, *144*, 217–234. [[CrossRef](#)]
29. Woodcock, C.E.; Loveland, T.R.; Herold, M.; Bauer, M.E. Transitioning from change detection to monitoring with remote sensing: A paradigm shift. *Remote Sens. Environ.* **2020**, *238*, 111558. [[CrossRef](#)]
30. Ye, S.; Rogan, J.; Zhu, Z.; Hawbaker, T.J.; Hart, S.J.; Andrus, R.A.; Meddens, A.J.H.; Hicke, J.A.; Eastman, J.R.; Kulakowski, D. Detecting subtle change from dense Landsat time series: Case studies of mountain pine beetle and spruce beetle disturbance. *Remote Sens. Environ.* **2021**, *263*, 16. [[CrossRef](#)]
31. Zhao, K.G.; Wulder, M.A.; Hu, T.X.; Bright, R.; Wu, Q.S.; Qin, H.M.; Li, Y.; Toman, E.; Mallick, B.; Zhang, X.S.; et al. Detecting change-point, trend, and seasonality in satellite time series data to track abrupt changes and nonlinear dynamics: A Bayesian ensemble algorithm. *Remote Sens. Environ.* **2019**, *232*, 20. [[CrossRef](#)]
32. Brooks, E.B.; Yang, Z.Q.; Thomas, V.A.; Wynne, R.H. Edyn: Dynamic Signaling of Changes to Forests Using Exponentially Weighted Moving Average Charts. *Forests* **2017**, *8*, 304. [[CrossRef](#)]
33. Capizzi, G.; Masarotto, G. An adaptive exponentially weighted moving average control chart. *Technometrics* **2003**, *45*, 199–207. [[CrossRef](#)]
34. Shu, L.J. An adaptive exponentially weighted moving average control chart for monitoring process variances. *J. Stat. Comput. Simul.* **2008**, *78*, 367–384. [[CrossRef](#)]
35. Simoes, B.F.T.; Epprecht, E.K.; Costa, A.F.B. Performance Comparisons of EWMA Control Chart Schemes. *Qual. Technol. Quant. Manag.* **2010**, *7*, 249–261. [[CrossRef](#)]
36. Roy, D.P.; Wulder, M.A.; Loveland, T.R.; Woodcock, C.E.; Allen, R.G.; Anderson, M.C.; Helder, D.; Irons, J.R.; Johnson, D.M.; Kennedy, R.; et al. Landsat-8: Science and product vision for terrestrial global change research. *Remote Sens. Environ.* **2014**, *145*, 154–172. [[CrossRef](#)]
37. Jin, S.M.; Yang, L.M.; Danielson, P.; Homer, C.; Fry, J.; Xian, G. A comprehensive change detection method for updating the National Land Cover Database to circa 2011. *Remote Sens. Environ.* **2013**, *132*, 159–175. [[CrossRef](#)]
38. Brooks, E.B.; Thomas, V.A.; Wynne, R.H.; Coulston, J.W. Fitting the Multitemporal Curve: A Fourier Series Approach to the Missing Data Problem in Remote Sensing Analysis. *IEEE Trans. Geosci. Remote Sens.* **2012**, *50*, 3340–3353. [[CrossRef](#)]
39. Aly, A.A.; Hamed, R.M.; Mahmoud, M.A. Optimal design of the adaptive exponentially weighted moving average control chart over a range of mean shifts. *Commun. Stat. Simul. Comput.* **2016**, *46*, 890–902. [[CrossRef](#)]
40. Tang, A.; Castagliola, P.; Hu, X.; Sun, J. The performance of the adaptive EWMA median chart in the presence of measurement error. *Qual. Reliab. Eng. Int.* **2019**, *35*, 423–438. [[CrossRef](#)]
41. Su, Y.; Shu, L.J.; Tsui, K.L. Adaptive EWMA procedures for monitoring processes subject to linear drifts. *Comput. Stat. Data Anal.* **2011**, *55*, 2819–2829. [[CrossRef](#)]
42. Haq, A.; Gulzar, R.; Khoo, M.B.C. An efficient adaptive EWMA control chart for monitoring the process mean. *Qual. Reliab. Eng. Int.* **2018**, *34*, 563–571. [[CrossRef](#)]
43. Wu, L.; Liu, X.N.; Liu, M.L.; Yang, J.H.; Zhu, L.H.; Zhou, B.T. Online Forest Disturbance Detection at the Sub-Annual Scale Using Spatial Context From Sparse Landsat Time Series. *IEEE Trans. Geosci. Remote Sens.* **2022**, *60*, 14. [[CrossRef](#)]

44. Li, Y.T.; Wu, Z.Z.; Xu, X.; Fan, H.; Tong, X.J.; Liu, J. Forest disturbances and the attribution derived from yearly Landsat time series over 1990-2020 in the Hengduan Mountains Region of Southwest China. *For. Ecosyst.* **2021**, *8*, 73. [[CrossRef](#)]
45. Cardille, J.A.; Perez, E.; Crowley, M.A.; Wulder, M.A.; White, J.C.; Hermosilla, T. Multi-sensor change detection for within-year capture and labelling of forest disturbance. *Remote Sens. Environ.* **2022**, *268*, 112741. [[CrossRef](#)]
46. Mahmoud, M.A.; Zahran, A.R. A Multivariate Adaptive Exponentially Weighted Moving Average Control Chart. *Commun. Stat.—Theory Methods* **2010**, *39*, 606–625. [[CrossRef](#)]
47. Lowry, C.A.; Woodall, W.H.; Champ, C.W.; Rigdon, S.E. A Multivariate Exponentially Weighted Moving Average Control Chart. *Technometrics* **1992**, *34*, 46–53. [[CrossRef](#)]
48. Bakdi, A.; Kouadri, A.; Bensmail, A. Fault detection and diagnosis in a cement rotary kiln using PCA with EWMA-based adaptive threshold monitoring scheme. *Control. Eng. Pract.* **2017**, *66*, 64–75. [[CrossRef](#)]
49. Aly, A.A.; Mahmoud, M.A.; Hamed, R. The Performance of the Multivariate Adaptive Exponentially Weighted Moving Average Control Chart with Estimated Parameters. *Qual. Reliab. Eng. Int.* **2016**, *32*, 957–967. [[CrossRef](#)]
50. Haq, A.; Khoo, M.B.C. An adaptive multivariate EWMA chart. *Comput. Ind. Eng.* **2019**, *127*, 549–557. [[CrossRef](#)]
51. Haq, A.; Khoo, M.B.C. A novel partially parameter-free adaptive multivariate EWMA mean chart. *Qual. Reliab. Eng. Int.* **2021**, *38*, 574–591. [[CrossRef](#)]
52. Wang, Z.; Wei, C.Y.; Liu, X.N.; Zhu, L.H.; Yang, Q.; Wang, Q.Y.; Zhang, Q.; Meng, Y.Y. Object-based change detection for vegetation disturbance and recovery using Landsat time series. *GISci. Remote Sens.* **2022**, *59*, 1706–1721. [[CrossRef](#)]
53. Hussain, M.; Chen, D.M.; Cheng, A.; Wei, H.; Stanley, D. Change detection from remotely sensed images: From pixel-based to object-based approaches. *ISPRS J. Photogramm. Remote Sens.* **2013**, *80*, 91–106. [[CrossRef](#)]

Disclaimer/Publisher’s Note: The statements, opinions and data contained in all publications are solely those of the individual author(s) and contributor(s) and not of MDPI and/or the editor(s). MDPI and/or the editor(s) disclaim responsibility for any injury to people or property resulting from any ideas, methods, instructions or products referred to in the content.